ARL-TR-10146 ● AUG 2025

Back-grinding Metallic Polycrystals for Improved X-ray Diffraction Patterns

by Braden L. Miller, Joshua M. Cline, Michael T. Hurst, James D. Paramore, Anup Bandyopadhyay, Eli Norris, Trevor Hastings, Ibrahim Karaman, Raymundo Arróyave, George M. Pharr, and Brady G. Butler

NOTICES

Disclaimers

The findings in this report are not to be construed as an official Department of the Army position unless so designated by other authorized documents.

Citation of manufacturer's or trade names does not constitute an official endorsement or approval of the use thereof.

Destroy this report when it is no longer needed. Do not return it to the originator.

ARL-TR-10146 ● AUG 2025

Back-grinding Metallic Polycrystals for Improved X-ray Diffraction Patterns

Braden L. Miller, Joshua M. Cline, Michael T. Hurst, James D. Paramore, Anup Bandyopadhyay, Eli Norris, Trevor Hastings, Ibrahim Karaman, Raymundo Arróyave, and George M. Pharr
Texas A&M University

Brady G. Butler
DEVCOM Army Research Laboratory

REPORT DOCUMENTATION PAGE

1. REPORT DATE	2. REPORT TYPE	3. DATES COVERED	
		START DATE	END DATE
August 2025	Technical Report	15 February 2024	01 January 2025

4. TITLE AND SUBTITLE
Back-grinding Metallic Polycrystals for Improved X-ray Diffraction Patterns

5a. CONTRACT NUMBER	5b. GRANT NUMBER	5c. PROGRAM ELEMENT NUMBER
W911NF-22-F-0032		
5d. PROJECT NUMBER	**5e. TASK NUMBER**	**5f. WORK UNIT NUMBER**

6. AUTHOR(S)
Braden L. Miller, Joshua M. Cline, Michael T. Hurst, James D. Paramore, Anup Bandyopadhyay, Eli Norris, Trevor Hastings, Ibrahim Karaman, Raymundo Arróyave, George M. Pharr, Brady G. Butler

7. PERFORMING ORGANIZATION NAME(S) AND ADDRESS(ES)	8. PERFORMING ORGANIZATION REPORT NUMBER
DEVCOM Army Research Laboratory ATTN: FCDD-RLA-MF Aberdeen Proving Ground, MD 21005	ARL-TR-10146

9. SPONSORING/MONITORING AGENCY NAME(S) AND ADDRESS(ES)	10. SPONSOR/MONITOR'S ACRONYM(S)	11. SPONSOR/MONITOR'S REPORT NUMBER(S)

12. DISTRIBUTION/AVAILABILITY STATEMENT
DISTRIBUTION STATEMENT A. Approved for public release: distribution unlimited.

13. SUPPLEMENTARY NOTES
ORCIDs: Braden L. Miller, 0009-0004-0382-2699; Joshua M. Cline, 0009-0007-6140-0234; Michael T. Hurst, 0000-0002-6138-2634; James D. Paramore, 0000-0001-8058-7662; Eli Norris, 0000-0003-4160-7194; Trevor Hastings, 0000-0003-4614-7019; Ibrahim Karaman, 0000-0001-6461-4958; Raymundo Arróyave, 0000-0001-7548-8686; George M. Pharr, 0000-0002-6634-8320; Brady G. Butler, 0000-0002-7677-9685

14. ABSTRACT
The advancements made in X-ray diffractometer technology and the equations that were developed over the course of the 20th century have made modern X-ray diffraction (XRD) a quick and reliable technique for characterizing a material's structure. Conventional sample types for XRD are monocrystals or powders; however, plenty of work has been done with polycrystalline materials. Each sample type has its own nuances: for polycrystals, grain size and orientation can cause issues during XRD experiments, and coarse grains and preferred orientations can lead to very few scanned crystallites that satisfy the Bragg criterion. This ultimately leads to low signal-to-noise ratios, missing peaks, and poor intensities in a scan. These issues can be compensated for by utilizing a simple back-grinding technique to increase the number of orientations that are queried during a scan. In this effort, a batch of coarse-grained high-entropy alloys were back-ground on two sizes of silicon carbide abrasive pads to decrease the crystallite sizes and increase the orientations that satisfy the Bragg criterion during a scan. This introduces some peak-broadening; however, it also significantly improves the XRD patterns and results in more useful data.

15. SUBJECT TERMS
X-ray diffraction, XRD, microstructure, Rietveld refinement, surface grinding, Sciences of Extreme Materials

16. SECURITY CLASSIFICATION OF:			17. LIMITATION OF ABSTRACT	18. NUMBER OF PAGES
a. REPORT	b. ABSTRACT	C. THIS PAGE		
UNCLASSIFIED	UNCLASSIFIED	UNCLASSIFIED	UU	22

19a. NAME OF RESPONSIBLE PERSON	19b. PHONE NUMBER *(Include area code)*
Brady G. Butler	(520) 691-5844

STANDARD FORM 298 (REV. 5/2020)
Prescribed by ANSI Std. Z39.18

Contents

List of Figures

1. Introduction

Crystal structure and microstructure are foundational in understanding the properties and performance of a material. The periodic arrangement of atoms, or crystalline structure, dictates many fundamental properties, which in turn dictates potential applications. For instance, the crystal structure influences a material's thermal, mechanical, and electrical properties.[1–7] Conversely, microstructure addresses structure at a larger length-scale—describing the arrangement, size, orientation, and distribution of crystal structures within a material. Microstructure can also have a significant influence on mechanical properties; refined grains are known to improve strength and toughness. However, controlling and refining microstructure can also influence our ability to measure crystal structure using conventional X-ray diffraction (XRD) techniques.[8–12]

This study stems from a broader investigation to discover single-phase refractory high-entropy alloys (HEAs) conforming to a specific crystal structure (i.e., body-centered cubic [BCC] using high-throughput methods).[13,14] The need to measure structural information in a high-throughput manner led the project to XRD, given its ability to verify that the samples are single-phase BCC materials, which was a foundational constraint in this materials-development effort. XRD was selected as one of the primary characterization methods for the high-throughput project, given its speed, reliability, and ability to confirm purity and structural details. However, coarse-grained materials present a significant challenge in XRD analysis; poor sampling of crystal orientations can lead to incomplete diffraction patterns, limiting the accuracy of phase identification. To address this, we introduce a simple yet effective approach (i.e., surface grinding of metallographic samples to improve the reliability of diffraction indexing). This method enhances the range of accessible orientations, producing diffraction patterns that more closely resemble those obtained in powder diffraction, a technique that has played a pivotal role in crystallography since its inception.[15,16]

Early XRD studies faced a fundamental limitation: high-quality single crystals were difficult to prepare, and their diffraction patterns were not always representative of the bulk material. In response, two independent research groups—one led by Paul Scherrer and Peter Debye and another led by Albert Hull—started investigating the use of powdered materials for XRD. Instead of relying on the problematic single crystals, they would grind materials into fine powders and use them to generate XRD rings. This would make material characterization via XRD more straightforward and accessible. Ultimately, they were successful in their endeavors and laid the foundation for modern XRD-based characterization of polycrystalline materials. Other contributors to the development of modern XRD-based methods

are William and Lawrence Bragg, whose work led to the development of the Bragg equation (a.k.a., Bragg's law).[16,17]

When using XRD to determine the structure of a material, Bragg's law, as shown in Equation 1, is one of the most important tools for analyzing the diffraction patterns of samples.

$$n\lambda = 2d\sin(\theta) \quad (1)$$

Where n is the diffraction order, λ is the wavelength, d is the spacing between crystal planes, and θ is the angle between the incident ray and the atomic plan or one-half of the angle between the emitter and detector. Through solving Bragg's law for a given θ and λ, it is possible to find the spacing between planes, d. The spacing of planes can then be used along with the plane geometries to solve for the lattice parameters of a unit cell. Additionally, due to the way that electromagnetic waves such as X-rays propagate and the principle of wave interference, Bragg's law also shows what is sometimes called the Bragg criterion. This criterion refers to the specific incident angles where the X-rays will constructively interfere since they are in phase with each other. This constructive interference is what leads to the characteristic XRD peaks seen in intensity versus two-theta (2θ) plots. In a coarse-grained sample, it may not be possible to query enough grains with orientations that satisfy the Bragg criterion. It is even possible that the grains scanned in an XRD run are oriented such that expected peaks do not appear since there were no orientations of those planes that satisfied the criterion. The samples used in this project were coarse-grained, which provided poor-quality scans due to the low number of orientations that satisfy the Bragg criterion. Our approach of surface back-grinding revives the foundational logic of early powder diffraction. Namely, that randomized crystallite orientation improves diffraction completeness. Where Debye and Hull turned to powders to address orientation bias, we restore that randomness via surface conditioning, without sacrificing the integrity of bulk samples. This process produced significant improvements over the original scans while introducing minimal error to the XRD measurements.[15–17]

The back-grinding process is widely applicable for coarse-grained samples, especially when trying to improve XRD results without destroying the specimen. This is quite useful, as there is currently much interest in refractory HEAs. These alloys tend to phase segregate and form dendritic microstructures instead of forming a solid solution.[18,19] Frequently, the solution to these issues is a very long, high-temperature homogenization heat treatment. However, such heat treatments trigger a significant amount of grain growth in these samples.[20–22] In some ways, the back-grinding process is a callback to traditional XRD methods, as well as an improvement upon them, as it involves making the surface of a bulk sample more

powder-like without destroying the entire sample. It is also easily implemented into a high-throughput workflow as it essentially just moves the XRD step to an earlier spot in the flow.

2. Methods

Batchwise-Bayesian optimization was used to select refractory HEA sample compositions based on several criteria. Once sample compositions were selected, sample microstructures were predicted to be single-phase BCC alloys by CALculation of PHAse Diagrams (CALPHAD) modeling. The samples were fabricated using vacuum arc melting and subsequently homogenized at high temperature (1925 °C) to refine the microstructure and minimize phase segregation.[23] This method successfully created homogenous single-phase alloys with a coarse grain structure.

Each sample was mounted in a conductive hot-mount powder consisting of graphite and phenol-formaldehyde using a hot mounting press (Allied High Tech TechPress 3). Samples were polished, 12 at a time, using a semiautomatic polishing machine (Allied High Tech MetPrep 4 with an AD-5 automatic fluid dispenser) using successively finer grits of silicon carbide, diamond suspensions, and finishing with 0.04-μm colloidal silica according to the procedures developed in this project.[23] This polishing procedure resulted in a smooth, metallographic finish for each sample that was suitable for subsequent imaging and nanoindentation studies.

The XRD scans of each sample were performed on a Bruker D8X-Discover XRD machine with an approximately 1-mm spot size and approximately 2-mm scanning area depending on the size of the specimen. Each scan went through a 2θ range of 30° to 110° and had the background signal subtracted from each profile. The initial XRD scans were carried on the mirror finish samples. After the first XRD scans, each sample was back-ground on a 12-inch-diameter 320-grit silicon carbide pad for 30 s with 5 lbf per puck. The samples were then sent to XRD to be rescanned. After the second XRD scans, each sample was back-ground once more using a 12-inch-diameter 180-grit silicon carbide pad and the same parameters as the 320-grit back-grinding. After the second back-grinding pass, the samples were scanned using XRD for the final time.

Rietveld refinements were performed on all XRD patterns from each batch, except for some mirror finish samples due to the pattern being too noisy and low intensity to get a good fit. The refinements were done using Profex 5.4.0,[24,25] an open-source diffraction pattern refinement software. A BCC tungsten structure file from the Crystallography Open Database was used as a baseline for the refinements since the compositions should result in a BCC lattice structure and the refinements were

not being used to calculate phase fractions.[26–28] The refinements only used lattice parameter, crystallite size, and sample displacement.

To characterize the surface damage caused by the back-grinding process, a single representative specimen (B20) was used to create cross sections of the back-ground surfaces. The sample was cut into three sections, which were remounted and prepared so that there was a sample for each finish: mirror, 320 grit, and 180 grit. These samples were subsequently remounted such that the cross section would be visible and polished to a mirror finish for scanning electron microscope (SEM) imaging. The cross sections of the back-ground specimens were imaged in a ThermoFisher Phenom XL using backscatter mode. The depth of the subsurface damage was measured using ImageJ to draw lines spanning the damaged region and recording the length of the lines in microns.

3. Results

The XRD data for the 24 mirror finish specimens showed poor signal-to-noise ratios and had misaligned or missing peaks (Figure 1). After the samples went through the 320-grit back-grinding, another round of XRD scans was performed. The 320-grit scans showed significant improvement in indexability over the mirror finish scans. As shown in Figure 1, the poor signal-to-noise ratio scans returned usable data after the samples were back-ground. Additionally, some of the missing peaks appeared and the intensities of most peaks improved. Despite significant improvements over the mirror finish scans, there was still information missing from the 320-grit scans. The 180-grit XRD scans showed more improvements over the mirror finish and 320-grit scans. All expected peaks were present and in locations consistent with a BCC structure, though some peaks still had low intensities or slight misalignments.

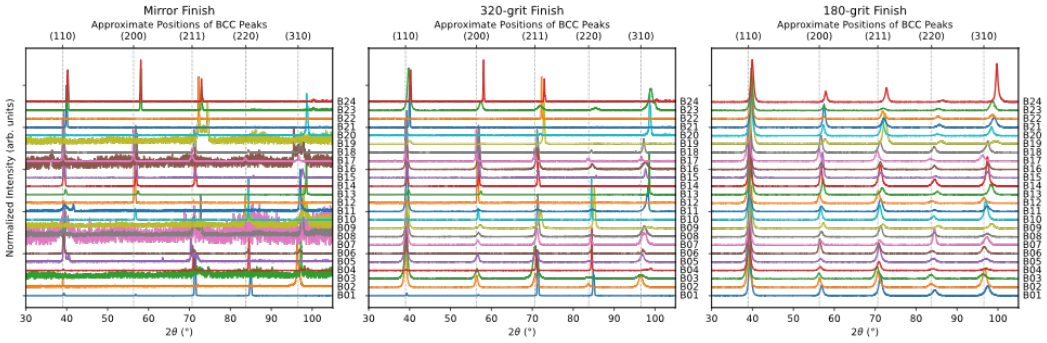

Figure 1. Three plots showing XRD patterns for a batch of 24 samples of varying composition produced in this material discovery effort. Normalized diffraction patterns are shown for the highly polished (Mirror Finish) and back-ground (320-grit and 180-grit) finishes, respectively.

While there were some undesired effects from the damage to the samples, the improvements in peak intensity presented in Figure 1 are obvious. As the scanned surface got rougher, the missing peaks started to appear, and the intensities of the peaks improved. The subsurface damage observed in the cross-sectioned samples is shown in Figure 2.

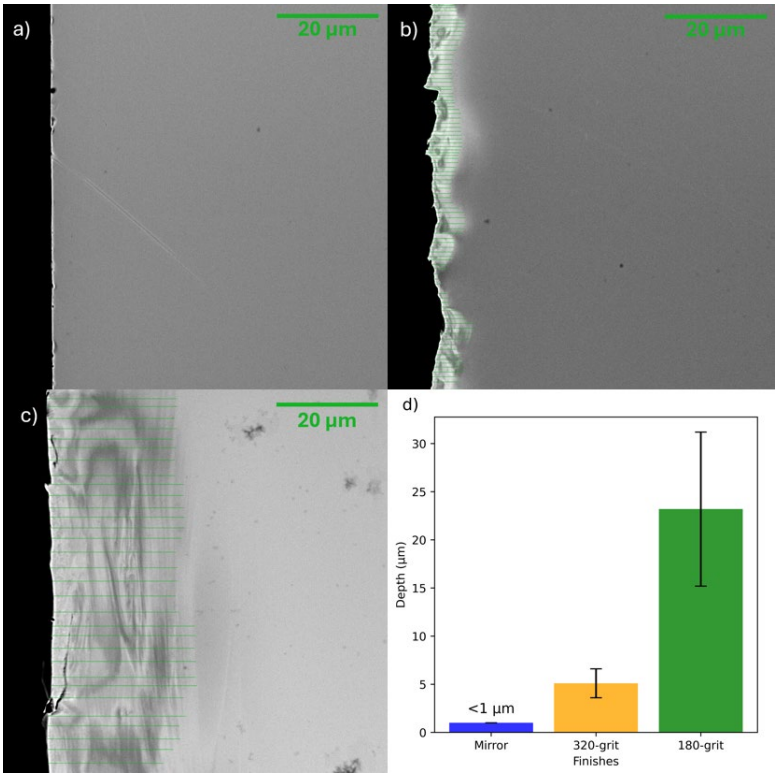

Figure 2. Polished cross sections of B20 showing a) mirror finish, b) 320-grit finish, c) 180-grit finish, and d) bar chart showing the depths of the subsurface damage.

The damaged layer on the 320-grit sample extended 5.1 ± 1.5 µm from the back-ground surface into the sample. On the 180-grit sample, the damaged layer

extended 23.2 ± 8.0 μm into the sample. Note that subsurface damage is not observable in the mirror finish sample (Figure 2). In addition to the subsurface damage, increasing amounts of peak broadening were observed in the XRD scans as the surface finish became rougher, as shown by Figure 3.

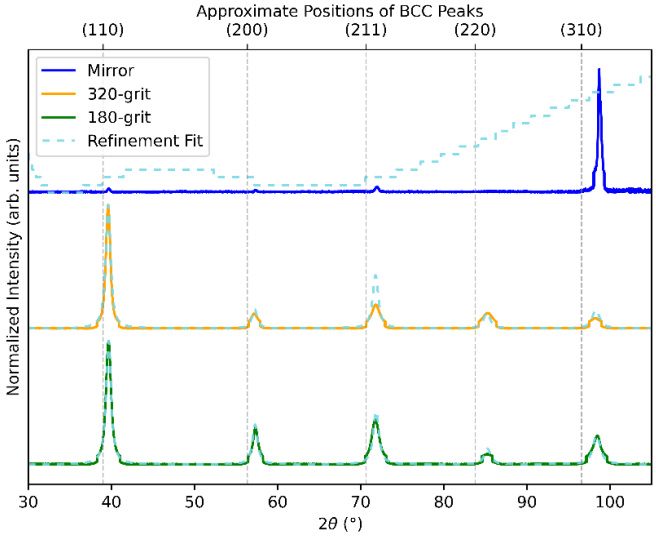

Figure 3. XRD scans for the three surface finishes on sample B20 demonstrating the improvement and peak-broadening introduced by the back-grinding process as well as the quality of the Rietveld refinements.

The Rietveld refinements were used to calculate the lattice parameters and approximate crystallite sizes. Additionally, the theoretical lattice parameter was calculated using molar volume data from ThermoCalc predictions. All lattice parameters are shown in Figure 4.

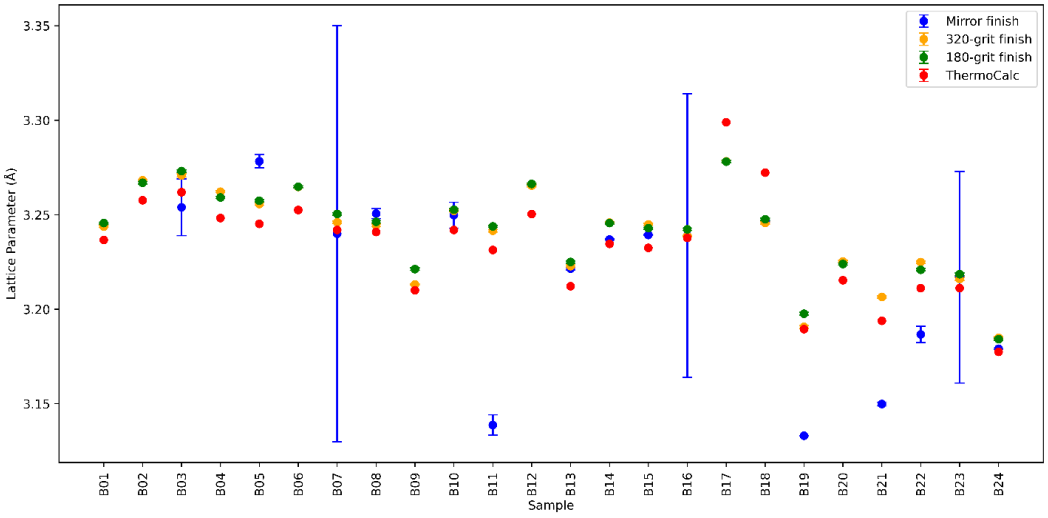

Figure 4. Plot showing the lattice parameters found through Rietveld refinements and their estimated lattice parameters based on ThermoCalc molar volume data.

The Rietveld refinements were also used to estimate the crystallite sizes of the material for the scanned areas. The correlation between the theoretical lattice parameters and the lattice parameters from the Rietveld refinements is high and indicates that the back-grinding process does not significantly distort the information in the XRD scans. Figure 5 shows a backscattered electron image that provides an example of the grain sizes in the mirror finish samples and the average crystallite size for each finish.

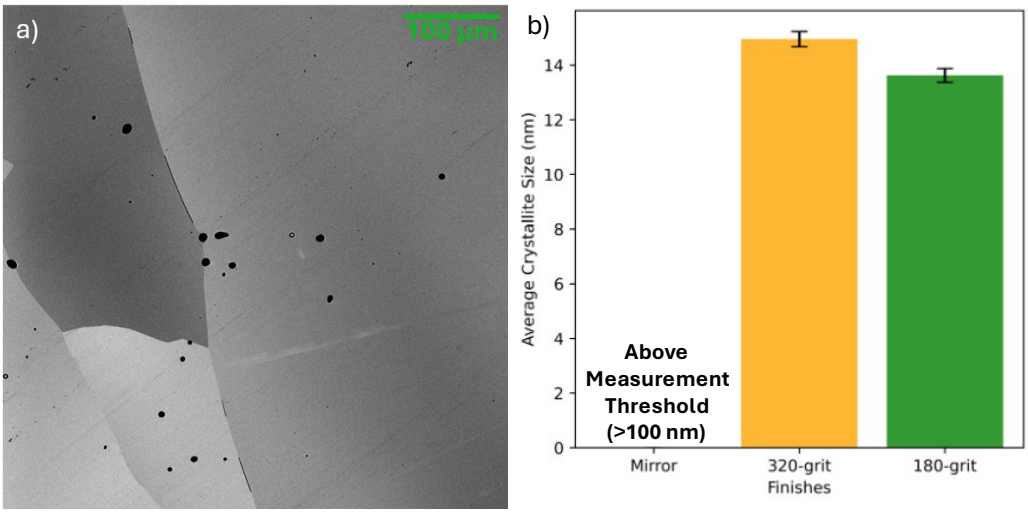

Figure 5. a) BSD image showing the large grains in sample B20. b) Bar chart showing the average crystallite size and average estimated standard deviation for each surface finish.

As shown in Figure 5, the 320-grit and 180-grit finish samples had average crystallite sizes of 14.95 ± 0.28 nm and 13.62 ± 0.25 nm, respectively. The mirror finish had crystallite sizes that were well above the measurement threshold, as shown by the BSD image in Figure 5.There was some porosity in the samples, but overall concentration of pores was not significant enough to influence the XRD results. The increase in surface roughness and the reduction in crystallite size in the scanned area is the likely cause of the peak-broadening observed in Figures 1 and 3.

4. Discussion

The methods used for synthesis of the samples result in very coarse microstructures. Multicomponent samples frequently have a broad solidification temperature range, which can result in dendritic structures. Although our alloy development strategy targeted materials with relatively narrow solidification ranges (i.e., $\Delta T = T_{solidus} - T_{liquidous} < 264.5$ °C),[13] a high-temperature homogenization treatment was required to keep compositions uniform and grain sizes greater than 200 µm were regularly observed. These coarse grains and the subsequent polishing to

prepare for SEM imaging and nanoindentation make the polished samples problematic for XRD methods.

The interaction depth of the XRD signal in bulk niobium was estimated based on attenuation of the incident X-ray beam at an incident angle corresponding to the Bragg condition for a 2θ angle of 40°. The attenuation depth (τ) was calculated using the material's linear attenuation coefficient. The mass attenuation coefficient (μ/ρ) for niobium at the copper Kα wavelength (λ = 1.5406 Å, 8.04 keV) is approximately 236 cm²/g,[29] and the density (ρ) of niobium is 8.57 g/cm^3, yielding a linear attenuation coefficient $\mu \approx 2024$ cm^{-1}. The characteristic attenuation depth (τ) is then given by

$$\tau = \frac{1}{\mu \sin(\theta)} \approx 1.44\ \mu\text{m}$$

This represents the depth at which the incident beam intensity falls to 37% of its surface value. However, the majority of diffracted signal arises from grains within approximately three attenuation depths (i.e., $3\tau = 95\%$ of the signal), corresponding to a maximum effective penetration depth of approximately 4.3 µm. This shallow interaction depth reflects the exponential attenuation behavior of X-rays in refractory metals, showing a highly limited depth of interaction. Accordingly, the signal in these refractory HEAs is dominated by lattice planes located within the top approximately 5 µm of the sample surface.

To estimate the number of grains contributing to the XRD signal, the projected beam footprint on the sample surface was calculated based on the beam diameter and the incident angle. For a circular beam with diameter D_b, the footprint becomes elliptical, with the major axis extended by a factor of $1/\sin\theta$, at an incident angle of $2\theta = 40°$, the area covered by beam diameters of 0.5, 1.0, and 2.0 mm, result in a projected area of 0.57, 2.27, and 9.07 mm^2.

Assuming grains are equiaxed, the average number of grains intersected by the beam footprint was estimated by dividing the projected beam area (A_b) by the average grain area (A_g), according to Equation 2:

$$N_{grains} = \frac{A_b}{A_g} = \frac{D_b^2}{\sin(\theta) D_g^2} \quad (2)$$

where D_g is the grain diameter. This can result in extremely poor sampling for conditions outlined in the range of this study. For example, a 1-mm-diameter beam interacting with a 200-µm grain size would intersect approximately 73 grains. The grain count increases quadratically with decreasing grain size and linearly with increasing beam area as shown in Figure 6.

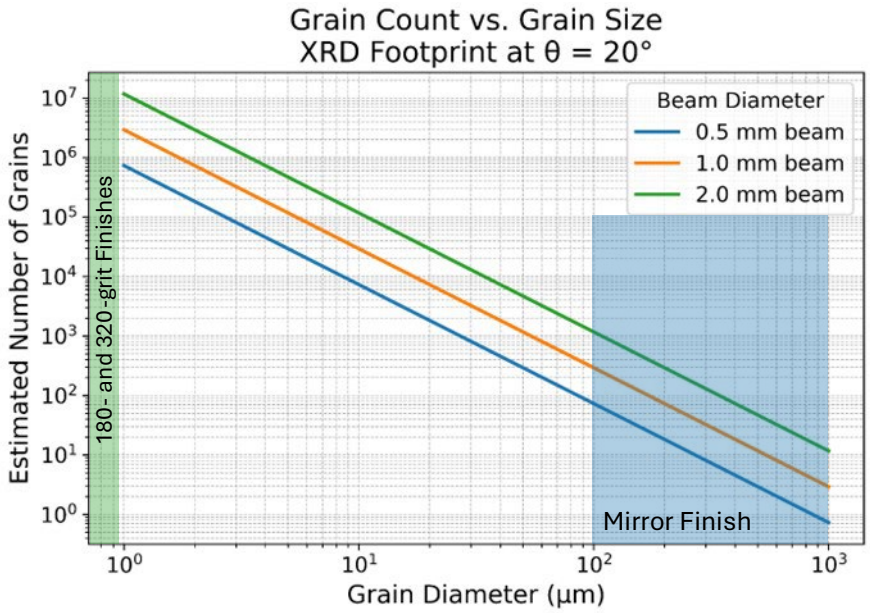

Figure 6. Estimation of the number of grains queried using 0.5–2.0 mm beam sizes for varying grain diameters. The shaded regions approximate the number of grains queried during the scans for each finish.

While no formal standard defines the minimum number of crystallites required to achieve representative Bragg diffraction in polycrystalline materials, prior work[30] suggests that good diffraction statistics are typically obtained when tens of thousands of randomly oriented grains are sampled. Using the prior approximation of the maximum effective penetration depth of 4.3 μm and observed depth of subsurface damage, it is apparent that the interaction volume of the beam does not extend past the damaged region in the 180-grit sample. This leads to many orientations being sampled, especially compared to the other two finishes, which corresponds with the observed increase in peak intensities.

Through the analysis of the three XRD sample batches, it was obvious that peak-broadening was occurring. This could be due to nanocrystalline regions created by the back-grinding process.[10,31–33] The lattice strain explanation is somewhat reinforced by the subsurface damage observed in the SEM micrographs shown by Figure 2, though the data is not sufficient to solidify the claim. Figure 5 shows that peak-broadening is tied to the creation of nanocrystalline regions during the back-grinding process. Despite these potentially problematic features, any subsurface damage or nanocrystalline regions can be easily removed by continuing the original grinding and polishing procedure for the specimen. This means that any coarse-grained sample could theoretically be sent for XRD scanning after being ground flat with a coarse abrasive, then polished to a mirror finish for other characterization after the XRD scan is completed.

Despite the peak-broadening and other effects of the back-grinding process, the lattice parameters found via Rietveld refinements for all back-ground finishes (that could be refined) are approximately the same as those of the polished samples. The refinement lattice parameters also agree well with the theoretical lattice parameters calculated based on ThermoCalc molar volume estimations for the samples, as shown by Figure 4. This makes it much easier to trust the lattice parameters returned from the Rietveld refinements and demonstrates that the peak broadening is not so severe that information is lost.

The back-grinding method serves as a practical homage to the original powder-diffraction techniques pioneered in the early 20th century. Just as Scherrer and Hull ground single crystals to access more diffraction vectors, we mechanically disturb the surface of coarse-grained samples to expand the set of orientations interrogated by the incident beam. The result is functionally similar: a pseudo-randomized surface microstructure yielding richer, more complete diffraction data. While traditional powder methods require destructively preparing a fine, randomized particulate, our approach achieves comparable orientation diversity in situ, making it ideal for high-throughput workflows or specimens requiring post-XRD characterization.

In addition to the improved XRD results, the lattice parameters from the Rietveld refinements showed promising correlation with the ones calculated based on ThermoCalc molar volume data. This was a nice confirmation as to the quality of the molar volume estimates provided by ThermoCalc as well as confirming that the lattice parameters found via Rietveld refinement were believable.

5. Conclusion

The original XRD data for the samples was poor, as coarse-grained samples are problematic for generating comprehensive diffraction patterns. While mirror finishes were essential for microscopy and nanoindentation, these samples were not suitable for our primary verification of the single-phase constraint outlined in our alloy development objective. This was easily solved using the back-grinding process due to the relative ease and minimal time investment. The back-grinding process caused peak broadening due to the generation of micro-/nano-crystalline regions and residual strains. Even with the peak broadening, the improvements in pattern quality are drastic and most secondary phases that were originally identified were still present in the deformed XRD patterns. This indicates that the broadening did not significantly affect the information collected from the back-ground samples. Despite these nuances, it is still a solution that is easily implemented as a first step

in a grinding/polishing procedure, and it is almost guaranteed to improve a coarse-grained sample's XRD results.

In essence, our back-grinding method does not replace powder diffraction but utilizes its core insight: randomness improves reliability in diffraction. Back-grinding can be utilized as a nondestructive, workflow-compatible process to improve phase identification in alloy development projects.

6. References

1. Nakagawa J et al. Crystal structure dependent thermal conductivity in two-dimensional phononic crystal nanostructures. Applied Physics Letters. 2015;107(2).
2. Li W et al. Crystal structure induced ultralow lattice thermal conductivity in thermoelectric Ag_9AlSe_6. Advanced Energy Materials. 2018;8(18):1800030.
3. Yan Q-L et al. The effect of crystal structure on the thermal reactivity of CL-20 and its C4-bonded explosives: part II. Models for overlapped reactions and thermal stability. Journal of Thermal Analysis and Calorimetry. 2013;112:837–849.
4. Aguadero A et al. Effect of Sr content on the crystal structure and electrical properties of the system La 2− × Sr × NiO 4+ δ (0≤ × ≤ 1). Dalton Transactions. 2006;(36):4377–4383.
5. Khanal GP et al. Effect of thermal annealing on crystal structures and electrical properties in $BaTiO_3$ ceramics. Journal of Applied Physics. 2018;124(3).
6. Callister WD, Rethwisch DG. Materials science and engineering: an introduction: SI version. 10th edition (global edition). Wiley; 2020. p. 834.
7. Wooster WA. Physical properties and atomic arrangements in crystals. Reports on Progress in Physics. 1953;16(1):62.
8. Ribárik G, Gubicza J, Ungár T. Correlation between strength and microstructure of ball-milled Al–Mg alloys determined by X-ray diffraction. Materials Science and Engineering: A. 2004;387–389:343–347.
9. Bindu P, Thomas S. Estimation of lattice strain in ZnO nanoparticles: X-ray peak profile analysis. Journal of Theoretical and Applied Physics. 2014;8(4):123–134.
10. Uvarov V, Popov I. Metrological characterization of X-ray diffraction methods for determination of crystallite size in nano-scale materials. Materials Characterization. 2007;58(10):883–891.
11. Chierchia R et al. Microstructure of heteroepitaxial GaN revealed by X-ray diffraction. Journal of Applied Physics. 2003;93(11):8918–8925.
12. Van Petegem S et al. On the microstructure of nanoporous gold: an X-ray diffraction study. Nano Letters. 2009;9(3):1158–1163.

13. Paramore JD et al. Two-shot optimization of compositionally complex refractory alloys. Acta Materialia. 2025;289:120820.

14. Mulukutla M et al. Illustrating an effective workflow for accelerated materials discovery. Integrating Materials and Manufacturing Innovation. 2024;13(2):453–473.

15. Etter M, Dinnebier RE. A century of powder diffraction: a brief history. Zeitschrift für anorganische und allgemeine Chemie. 2014;640(15):3015–3028.

16. Cullity BD, Stock SR. Elements of X-ray diffraction. 3rd ed. Prentice Hall; 2001.

17. Robotti N. The discovery of X-ray diffraction. Rendiconti Lincei. 2013;24(1):7–18.

18. Gao MC et al. Senary refractory high-entropy alloy HfNbTaTiVZr. Metallurgical and Materials Transactions A. 2016;47(7):3333–3345.

19. Miracle DB, Senkov ON. A critical review of high entropy alloys and related concepts. Acta Materialia. 2017;122:448–511.

20. Maiti S, Steurer W. Structural-disorder and its effect on mechanical properties in single-phase TaNbHfZr high-entropy alloy. Acta Materialia. 2016;106:87–97.

21. Senkov ON, Woodward C, Miracle DB. Microstructure and properties of aluminum-containing refractory high-entropy alloys. JOM. 2014;66(10):2030–2042.

22. Chen S et al. Grain growth and Hall-Petch relationship in a refractory HfNbTaZrTi high-entropy alloy. Journal of Alloys and Compounds. 2019;795:19–26.

23. Paramore JD et al. Two-shot optimization of compositionally complex refractory alloys. arXiv preprint; 2024. arXiv:2405.07130.

24. Profex – Open Source XRD and Rietveld Refinement. Profex.

25. Doebelin N, Kleeberg R. Profex: a graphical user interface for the Rietveld refinement program BGMN. Journal of Applied Crystallography. 2015;48(5):1573–1580.

26. Downs RT, Hall-Wallace M. The American mineralogist crystal structure database. American Mineralogist. 2003;88:247–250.

27. Grazulis S et al. Crystallography open database – an open-access collection of crystal structures. Journal of Applied Crystallography. 2009;42(4):726–729.

28. Dubrovinsky LS, Saxena SK. Thermal expansion of periclase (MgO) and tungsten (W) to melting temperatures. Physics and Chemistry of Minerals. 1997;24(8):547–550.

29. NIST. X-ray mass attenuation coefficients – niobium. https://physics.nist.gov/PhysRefData/XrayMassCoef/ElemTab/z41.html

30. Kleeberg R, Monecke T, Hillier S. Preferred orientation of mineral grains in sample mounts for quantitative XRD measurements: how random are powder samples? Clays and Clay Minerals. 2008;56(4):404–415.

31. Khelifi S et al. Correlations between XRD peak broadening and elastic and plastic deformation for mild steel sheets under tensile loading. Materials Science. 2024;30(3):414–422.

32. Zaidi UZM et al. Crystallite size and microstrain: XRD line broadening analysis of AgSiN thin films. Pigment & Resin Technology. 2018;48(6):473–480.

33. Biju V et al. Estimation of lattice strain in nanocrystalline silver from X-ray diffraction line broadening. Journal of Materials Science. 2008;43(4):1175–1179.

List of Symbols, Abbreviations, and Acronyms

BCC	body-centered cubic
CALPHAD	CALculation of PHAse Diagrams
HEA	high-entropy alloy
SEM	scanning electron microscope
XRD	X-ray diffraction

1 (PDF)	DEFENSE TECHNICAL INFORMATION CTR DTIC OCA
1 (PDF)	DEVCOM ARL FCDD RLB CI TECH LIB